SCIENCE CHINA
Technological Sciences

•Article•

https://doi.org/10.1007/s11431-022-2088-0

Shape optimization of corrugated tube using B-spline curve for convective heat transfer enhancement based on machine learning

SHI ChunYu, YU MinJie, LIU Wei & LIU ZhiChun*

School of Energy and Power Engineering, Huazhong University of Science and Technology, Wuhan 430074, China

Received March 5, 2022; accepted May 20, 2022; published online September 19, 2022

A significant way to achieve energy saving and emission reduction is to optimize the design of heat transfer devices. As is widely applied in industry, a corrugated tube constructed by B-spline curve is numerically investigated and the profile is optimized, using a surrogate model with considerations of performance evaluation criterion (*PEC*) as single objective or minimum flow resistance (*f*) and maximum Nusselt number (*Nu*) as multi-objective. The machine learning technique is used to determine the candidate samples to update the surrogate model for improving the optimization efficiency and reliability, which is validated to be effective in this paper. The optimization results show that the comprehensive performance of the corrugated tube is more sensitive to the vertical coordinates of the control points, with the appropriate increase in the number of control points for B-spline, and the better performance of corrugated tubes is achieved. The optimal profile corresponding to the best comprehensive performance is a double-crest shape. With Reynolds number (*Re*) increased, the wave-amplitude of the first wave gradually gets smaller, and the profile of the corrugated tube becomes smoother. With the increasing consideration of heat transfer performance over multi-objective optimization, the optimal shape gradually changes from a double-trough to a single-trough shape. Finally, the maximum *PEC* of 1.2415, 1.1845, and 1.1504 are acquired with the *Re* = 8000, 10000, and 12000, respectively, and the maximum *Nu* increases from 358.540 to 478.821. Compared with the design with the maximum thermal performance, the best compromise solution from multi-objective optimization is determined at *Re* = 8000, 10000, and 12000, showing improved flow resistance of 83.917%, 85.465%, and 84.473%, but with sacrificed thermal performance of 36.754%, 37.088%, and 35.005%, respectively.

convective heat transfer, corrugated tube, surrogate model, machine learning, numerical simulation

Citation: Shi C Y, Yu M J, Liu W, et al. Shape optimization of corrugated tube using B-spline curve for convective heat transfer enhancement based on machine learning. Sci China Tech Sci, 2022, 65, https://doi.org/10.1007/s11431-022-2088-0

1 Introduction

Energy conversion is an important issue in facilitating high-quality economic development and promoting the reduction of carbon dioxide emissions. Heat exchanger has a wide range of applications in various fields of industry, especially in supercritical CO_2 Brayton cycle [1,2] or chemical engineering [3]. The structure of the heat exchanger tube has a visible impact on improving the energy conversion efficiency, and many techniques and methods have been conducted to analyze the effective control of heat and mass transfer in tubes [4]. Passive heat transfer enhancement techniques are those that do not require any external power equipment which makes them more accessible for improving heat transfer efficiency. Generally, different structures are used in the destruction of the boundary layer and generating secondary flow, which include dimples [5–8], twisted tapes [9,10], porous inserts [11,12], and spiral tubes [13–15].

Owing to the advantages of simple structure and low cost, many previous studies have revealed that corrugated tube is characterized by a relatively advanced thermal performance compared with the conventional smooth tube. Because of the

*Corresponding author (email: zcliu@hust.edu.cn)

variety of corrugated tubes in industrial applications, scholars have investigated corrugations with different geometrical shapes. Akyildiz et al. [16] established a theoretical model and obtained analytical solutions for the temperature and velocity distributions in transversally corrugated pipes. By comparing the temperature and velocity fields in tubes with the transversally corrugated cross-section with the different number of peaks n_p and amplitude ε, they found that the friction factor and the heat transfer rate both become smaller with the increasing n_p and ε. Mohammed et al. [17] described a numerical investigation to study the effects of rectangular corrugation parameters on the hydraulic-thermal performance through transversely corrugated circular tubes. They pointed out that both the highest Nusselt number and friction factor are obtained in the case of lowest pitch and highest height of corrugations, and there is an optimum *PEC* at rib height $e = 0.25$ mm, rib pitch $p_r = 5$ mm, rib width $w_r = 2$ mm. Ajeel et al. [18–20] performed a comparison study on the thermal performance of different corrugated channels, namely, semicircle corrugated channel, trapezoidal corrugated channel, and straight channel. It was observed that turbulent kinetic energy is heavily dependent on the form of corrugation, and a maximum improvement of 12.87% on the heat transfer rate was obtained. Ahmed et al. [21] presented their numerical research and analyzed the effect of geometrical parameters for trapezoidal corrugations on the temperature and velocity distributions. They observed that the average Nusselt number was enhanced with the increasing amplitude of corrugation due to the higher temperature gradient near the wall caused by the mixing of fluid. Al-Obaidi and Alhamid [22] conducted a numerical study on the improvement of heat transfer of tubes with varying arc ring configurations and found the highest value of *PEC* is more than 1.3 under the Reynolds number of 4000. The sinusoidal-wavy channel was analyzed numerically and experimentally by Khoshvaght-Aliabadi et al. [23,24]. It was concluded that, beyond the wavelength, the wave height has the most significant effect on heat transfer characteristics. Zhang et al. [25] proposed a circumscribed arc-wave wall tube, whose wall is composed of two semi-circular arcs with different radiuses and further investigated the heat transfer characteristics under a pulsating flow field. They found that the heat transfer capacity of the corrugated tube is affected by the radius ratio i. The smaller the i, the greater the heat transfer is. Pethkool et al. [26] designed an experimental procedure for understanding the augmentation of convective heat transfer by using helically corrugated tubes, exhibiting the maximum improvement on heat transfer rate as high as 232% for the corrugations with the pitch-to-diameter ratio $p/D_H = 0.27$, and height-to-diameter $e/D_H = 0.06$. Verma et al. [27] carried out an experimental study on the heat transfer characteristics of a helically corrugated tube and found that the maximum heat transfer efficiency is acquired when the corrugation depth is set as 4 mm. Hong et al. [28] designed a new wave corrugated tube with the corrugated strips distributed sinusoidally along the circumference, showing excellent heat transfer performance due to the improved flow mixing and the generations of multi-longitudinal vortices induced by the corrugations. Begag et al. [29] analyzed the enhancement of heat transfer by replacing smooth tubes with V-shaped corrugated tubes. As a result, they succeeded in showing that the corrugations improved the thermal performance due to a larger heat transfer area, and a better Nusselt number was obtained when the concave corrugated tubes had a phase shift angle of 180°. Liao et al. [30] selected the skewness and kurtosis of the corrugations as design parameters to optimize the shape of the corrugations. They proposed that comprehensive performance gets better with the decrease in skewness and kurtosis.

In the past decades, a relatively better performance is achieved by comparing different parameter combinations. With the development of global optimization algorithms, numerous algorithms inspired by natural principles have been introduced, which has provided a wide range of facilities for the optimization of heat transfer devices, such as genetic algorithm [31–35], simulated annealing algorithm [36–40], particle swarm algorithm [41–45], and so on. However, due to the incremental complexity of physical problems and the constraint of computational resources, how establishing the mathematical correlations between the performance indicators and the design parameters has become a critical problem that limits the application of advanced optimization algorithms. The most popular method is to build a surrogate model to approximate the relationship between the inputs and the outputs, such as response surface model (RSM), radial basis function (RBF), and artificial neural network (ANN), which has the advantages of high optimization efficiency and ease of operation. Han et al. [46,47] performed an optimization for corrugated tubes inserted with multi-channel twisted tape. An RSM and genetic algorithm are used to optimize the design variables. Wang et al. [48–50] established an RSM to optimize a double pipe heat exchanger with an outward helically corrugated tube. The model is validated by comparing the predicted value with the experimental data, and the maximum error is less than 20%. Yu et al. [51] adopted 25 design points obtained by the central composite design to construct a response surface for the optimization of shell and tube heat exchangers with sinusoidal wavy tape. Milani Shirvan et al. [52] also used an RSM to optimize the heat exchanger with the corrugated tubes. Four effective parameters of the tube structure were chosen to obtain the best performance. Grabski and Kołodziej [53] established an RBF to analyze the thermal-hydraulic performance in an internally corrugated tube whose cross-section is described by a cosine function. Moreover, Yarmohammadi et al. [54] employed an ANN to build a

correlation between the heat transfer coefficient and design variables. Combined with the optimization algorithm, R-404A evaporation inside corrugated tubes is optimized. Moya-Rico et al. [55] presented an ANN for predicting the heat transfer characteristics of corrugated tubes and found that the results are in good agreement with the experimental results when two hidden layers have 15 and 21 nodes, respectively.

The above literature review shows that the structure of corrugations has an obvious improvement for the heat transfer and flow performance in the tubes. Scholars have proposed various corrugation designs with excellent performance. However, when making improvements for the corrugated tubes, scholars are used to determining the profile of corrugation as a certain shape firstly, regular shape or the deformation of the regular shape, which leads to many curves that do not satisfy the design form are not considered. And then they perform their optimizations only for the structural parameter which leads to the optimization range is much narrower. Additionally, some surrogate models cannot accurately characterize problems with high nonlinearity, and is powerless in handling problems with many design variables, which causes an inaccuracy acquisition of the best profile as the optimization algorithm is used.

B-spline curve is a curve generation method with the characteristics of simple generation and flexible adjustment, which can represent most of curves, regular or irregular curves, only by the position of the control points and the number of points. To find the best curve for the profile of the corrugated tube without any shape limitation, in this paper, B-spline curve is employed to determine the corrugation shape. The optimal profile and the effect of the control point number on the optimal profile are investigated. Meanwhile, the variation of the optimal profile as the Reynolds number increases is explored. A further multi-objective objective optimization is performed for the best compromise solution under the different heat transfer and flow resistance requirements. In order to solve the problems such as undesirable optimization results due to inaccurate predictions of the surrogates, a surrogate based on machine learning technique (SML) is constructed, and the optimization results are validated with the solutions obtained by directly coupling the CFD solver and genetic algorithm. The optimization method employed in the paper can be used in other thermal systems and the optimization results can be used to guide the production of the corrugated tube to improve energy conversion efficiency.

2 Computational model and solution strategy

2.1 Physical problem description

The geometry structure of the corrugated tube studied in the present numerical simulation is shown in Figure 1. The corrugation units are periodically arranged in the test section of the tube in order to improve the heat transfer rate, and a total of $N_c = 40$ periodic units is applied in the numerical model, and the length of the unit is $L_w = 10$ mm. Two smooth straight tubes with the lengths of $L_{in} = 200$ mm and $L_{out} = 400$ mm are arranged on the entry and outflow sections to eliminate the entrance effect and reversed flow in the outlet respectively. Accordingly, the total length of the domain is $L = 1000$ mm, the radius of the tube is $r_0 = 5$ mm. For the convenience of the present study, the tube is simplified to a 2D-axisymmetric model, so the shape of the wave structure is determined by a curve.

B-spline is a typical method of curve generation used in computer-aided design owing to its local modifiability and flexible control property, which is automatically generated by several control points. The curve is unique under the same control points, and $P(u)$ is defined as a polynomial spline function of kth degree given by [56]

$$P(u) = \sum_{i=0}^{n} P_i B_{i,k}(u), \tag{1}$$

where u is an independent value, and any point on the curve is expressed by modifying it. k is the degree of the curve, and generally, a higher k means a smoother curve, but a longer computation time. In general, the degree k is set to 3. P_i is the set of n control points and $B_{i,k}(u)$ is the B-spline basis function of degree k and defined as

$$B_{i,0}(u) = \begin{cases} 1, & \text{if } u_i \le u \le u_{i+1}, \\ 0, & \text{otherwise}, \end{cases} \tag{2}$$

$$B_{i,k}(u) = \frac{(u-u_i)B_{i,k-1}(u)}{u_{i+k}-u_i} + \frac{(u_{i+k+1}-u)B_{i+1,k-1}(u)}{u_{i+k+1}-u_{i+1}}. \tag{3}$$

u_i as the ith knot is determined by

$$u_i = \begin{cases} 0, & 0 \le i \le k+1, \\ i-k, & k+1 \le i \le n-1, \\ n-k, & n-1 \le i \le n+p. \end{cases} \tag{4}$$

It can be seen from eqs. (1)–(4) that the generation of B-spline curve is only determined by the positions and the number of control points when the degree k is determined. Therefore, the number of control points as well as the coordinates is selected as research parameters for determining the optimal profile of the corrugated tubes. Figure 1(c) gives exemplary cases of the corrugated tube constructed by B-spline curve of degree $k = 3$ and control points $n = 3$, $n = 5$, $n = 7$.

2.2 Governing equations and boundary conditions

In this study, water is chosen as the working fluid, and the flow is assumed to be steady, turbulent, Newtonian, and without viscous dissipation, whose physical properties are unchanged with temperature. Given that the velocity is in the

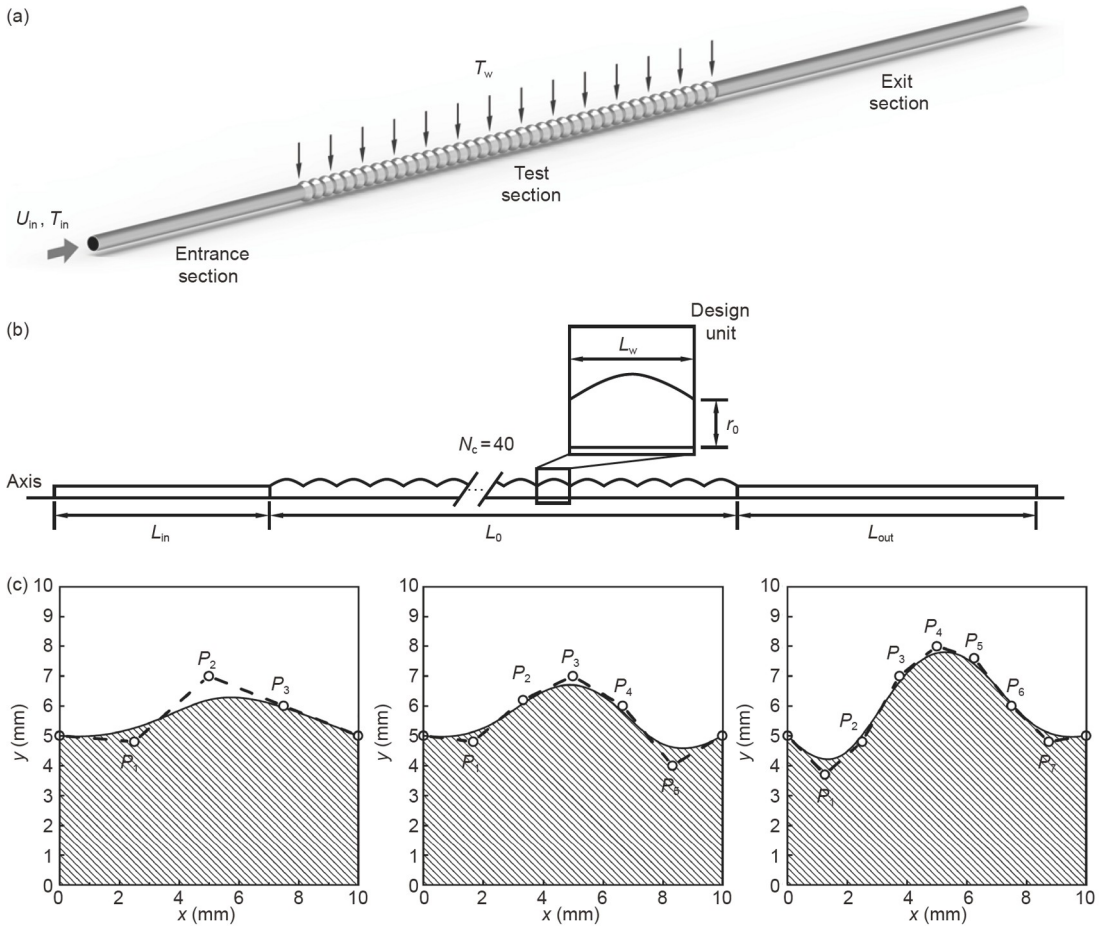

Figure 1 Schematic description of the geometry structure. (a) Physical model for corrugated tube; (b) calculated domain; (c) B-spline curve and control points.

range of 0.8–1.2 m/s and the Reynolds number is in the range of 8000–12000, the SST k-ω turbulence model is employed for the fluid region. The governing equations include the continuity, Reynolds averaged Navier-Stokes, energy, and turbulence model equations. In tensor form, the continuity, Navier-Stokes, and energy equations are [57]

$$\frac{\partial \rho u_j}{\partial x_j} = 0, \tag{5}$$

$$\frac{\partial}{\partial x_j}(\rho u_i u_j) = -\frac{\partial p}{\partial x_i} + \frac{\partial}{\partial x_j}\left[\mu\left(\frac{\partial u_i}{\partial x_j} + \frac{\partial u_j}{\partial x_i}\right)\right] - \frac{2}{3}\mu\frac{\partial u_i}{\partial x_j}\delta_{ij} + \frac{\partial}{\partial x_j}\left(-\rho\overline{u_i' u_j'}\right), \tag{6}$$

$$\frac{\partial}{\partial x_j}\left(\rho u_j C_p T\right) = \frac{\partial}{\partial x_j}\left(k_{\text{eff}}\frac{\partial T}{\partial x_i}\right). \tag{7}$$

The Reynolds stresses must be modeled to close eq. (6). The SST k-ω turbulence model developed from the standard k-ω model is suitable to use at low Reynolds numbers, which is adopted to ensure an accurate prediction of the near-wall conditions [58]. The details of the model are defined as

$$\frac{\partial}{\partial x_i}(\rho k u_i) = \frac{\partial}{\partial x_j}\left[\left(\mu + \frac{\mu_t}{\sigma_k}\right)\frac{\partial k}{\partial x_j}\right] + G_k - Y_k, \tag{8}$$

$$\frac{\partial}{\partial x_i}(\rho \omega u_i) = \frac{\partial}{\partial x_j}\left[\left(\mu + \frac{\mu_t}{\sigma_\omega}\right)\frac{\partial \omega}{\partial x_j}\right] + G_\omega - Y_\omega + D_\omega, \tag{9}$$

where σ_k, σ_ω, and μ_t are the turbulent Prandtl numbers for k and ω and the turbulent viscosity, respectively.

In this study, the calculations are numerically performed based on the finite volume method [59] by the platform, ANSYS Fluent 19.0. The second upwind scheme is employed to solve the intermediate point values of the algebraic equations after the discretization process. The pressure-velocity coupling field is obtained by the Semi-implicit technique for pressure-linked equations (SIMPLE) algorithm. The solution process is terminated and considered to be converged when the standardized residuals for the continuum equations, momentum equations, and energy equations are less than 10^{-6}, 10^{-6}, and 10^{-8}, respectively.

The boundary conditions defined at the inlet are uniform velocity u_{in} = 0.8–1.2 m/s and temperature T_{in} = 300 K, with a turbulent intensity of I = 5%. The pressure gauge of the

outlet is set as $P_{out} = 0$, defining the backflow turbulent intensity as $I = 5\%$. A no-slip boundary condition is applied to the convective heat transfer surfaces as the shear condition, and the temperature of which is fixed at $T_w = 333.15$ K.

2.3 Data reduction

The velocity and temperature fields can be obtained by numerical analysis. The friction factor (f) of the corrugated structure section is employed to characterize the hydraulic performance and it can be calculated from [60]

$$f = \frac{\Delta p}{N_c L_w} \frac{2r_0}{(1/2)\rho_f u_{in}{}^2}. \tag{10}$$

The corresponding Reynolds number (Re) is

$$Re = \frac{2\rho_f u_{in} r_0}{\mu_f}. \tag{11}$$

The Nusselt numbers (Nu) are chosen to evaluate the thermal performance, which can be calculated as [61]

$$Nu = \frac{2hr_0}{\lambda_f}, \tag{12}$$

where h is the heat transfer coefficient, which can be calculated as

$$h = \frac{q}{T_w - T_m}, \tag{13}$$

$$T_m = \frac{\int_0^{r_0} uTr\mathrm{d}r}{\int_0^{r_0} ur\mathrm{d}r}. \tag{14}$$

The performance evaluation criterion PEC is employed to evaluate the comprehensive performance of the heat transfer and flow resistance [62]:

$$PEC = \frac{Nu/Nu_{smooth}}{(f/f_{smooth})^{1/3}}. \tag{15}$$

2.4 Grid independence and model validation

Due to the simple structure of the 2D axisymmetric model for corrugated tubes, a structural quadrilateral mapping grid is employed in this paper. Figure 2 gives the grid schematic, and four randomly generated B-spline curves are used to confirm the applicability of the meshing method to arbitrary conditions. The grid in the corrugations is refined to capture local features, and the boundary layer grid is generated near the wall to ensure that the value of $y^+ < 1$. To improve the computational efficiency while ensuring the accuracy of the numerical process, the analysis of grid independence is employed to determine the minimum number of grids. With the corrugated tube of the same radius as the analysis object, five different grid systems are generated to check the grid independence namely, 20000, 38000, 60000, 84000, and 107000. The deviations of Nu and friction factor values are less than 0.1% when the number of grids exceeds 84000. Therefore, to save computational time, a mesh number of 84000 is selected for the simulations in this study.

Numerical validations are conducted according to the empirical formula for smooth tubes given in ref. [63]. Under the same working conditions, the Nusselt number and friction factor are chosen as comparative parameters with the eqs. (16) and (17), which are considered feasible in the range of Re from 2300 to 10^6. Subsequently, the results of the numerical calculation in the corrugated tube are compared with the experimental results of Hu et al. [64], which adopts air as the working fluid. Figure 3 shows that the numerical solutions are in good agreement with the theoretical results and the experimental results which prove that the numerical method used in this paper is accurate and effective.

$$Nu_{theo} = \frac{(f/8)(Re-1000)Pr_f}{1+12.7\sqrt{f/8}\left(Pr_f{}^{2/3}-1\right)}\left[1+\left(\frac{d}{l}\right)^{2/3}\right]c_t,$$
$$c_t = \left(\frac{Pr_f}{Pr_w}\right)^{0.01}, \tag{16}$$

$$f_{theo} = (1.82\lg Re - 1.64)^{-2}. \tag{17}$$

3 Surrogate and optimization method

3.1 Surrogate model based on machine learning

Surrogate model based on machine learning (SML) provides

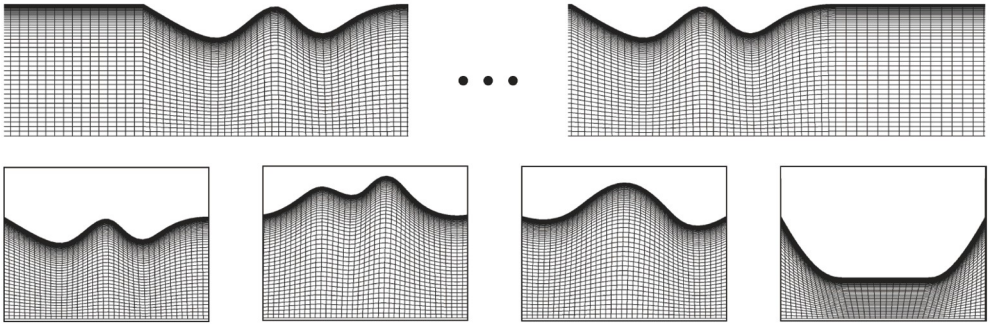

Figure 2 Mesh generation for corrugated tube.

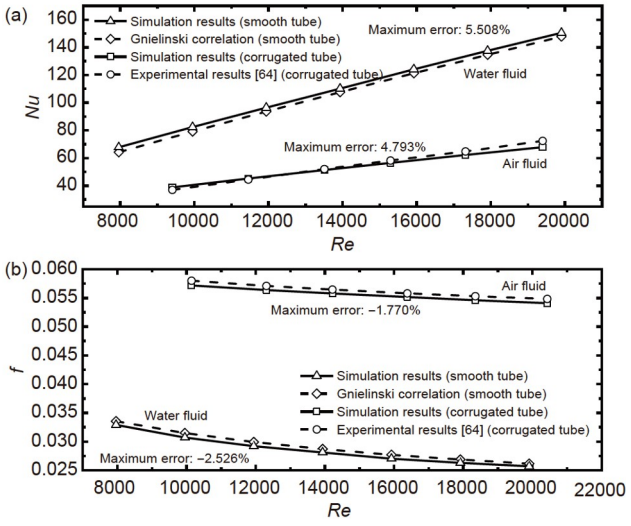

Figure 3 Validation of simulated results.

a strategy for improving the surrogate model to guide the efficient optimization of an unknown black-box function. The algorithm functions by building a rough surrogate model which is updated by adding candidate samples until the best value is found with no improvements. Compared with traditional surrogates, on the one hand, SML gives the desired results with fewer samples, which improves the optimization efficiency. On the other hand, continuous exploration helps us to find the neglected local features and reduces the impact of prediction errors on optimization results.

The main process of constructing SML is shown in Figure 4. Firstly, a small number of points are sampled and calculated by the above numerical method to receive the exact performance value. An initial surrogate is established by the parameters and performance of the samples. In this paper, the Kriging model is chosen as the surrogate model.

When the nonlinearity of the research problem is high, the initial model is unable to characterize the local features of the true distribution. For ensuring the reliability of the optimization results, the initial model needs to be updated by adding candidate points, but the selection of candidate points is an extremely complex problem. Improper selection can lead to less efficient optimization. A simple way to update the surrogate is determining the candidate point at the optimal value of the current surrogate, but when the optimization proceeds to a local optimum, the model fails to update. Another way is determining the candidate point at the maximum predicted error of the current surrogate, but it is difficult to the termination of the optimization process until all the points have been calculated. An acquisition function based on machine learning technique is required to guide the sampling direction, which uses statistical principles to determine the candidate point to improve the current model as much as possible. In this paper, the acquisition function is based on the expected improvement criterion

After the candidate sample is determined, the exact performance of the candidate sample is calculated by numerical method to enrich the sample sets and update the surrogate until the convergence condition is satisfied. In this paper, the convergence condition is that the maximum expected improvement value is less than 10^{-4}, and the optimal value does not change between 20 iterations of updating process.

3.1.1 *Kriging model*

The Kriging model (KRG) is a widely used surrogate model in engineering with high accuracy and flexibility [65,66]. In statistics, KRG is also called the Gaussian process model because it treats the objective function as a Gaussian process. Assuming that there are N sample points and the exact values of the sample points are calculated by the numerical simulation, KRG has the following form [67]:

$$\hat{f}(\mathbf{x}) = \mu + \epsilon(\mathbf{x}), \tag{18}$$

where μ is the mean value of the Gaussian process and $\epsilon(\mathbf{x})$ is the error term which conforms to a normal distribution with the mean of 0 and variance of σ^2. KRG considers the error terms at any two points to be correlated:

$$\begin{aligned}\mathbf{R}\left(\theta_k, \mathbf{x}^i, \mathbf{x}^j\right) &= \mathrm{Corr}[\epsilon(\mathbf{x}^i), \epsilon(\mathbf{x}^j)] \\ &= \exp\left(-\sum_{k=1}^{n} \theta_k \left|\mathbf{x}_k^i - \mathbf{x}_k^j\right|\right),\end{aligned} \tag{19}$$

where n represents the number of design variables. θ_k ($k = 1, 2, \ldots, n$) is the undetermined coefficient. The response value $\hat{y}(\mathbf{x})$ at the point $\mathbf{x}$ can be estimated according to KRG:

$$\hat{y}(\mathbf{x}) = \hat{\mu} + \mathbf{r}^{\mathrm{T}}\mathbf{R}^{-1}(\mathbf{y} - \mathbf{1}\hat{\mu}). \tag{20}$$

And the variance of predicted values:

$$s^2(\mathbf{x}) = \hat{\sigma}^2\left[1 - \mathbf{r}^{\mathrm{T}}\mathbf{R}^{-1}\mathbf{r} + \frac{(1 - \mathbf{1}^{\mathrm{T}}\mathbf{R}^{-1}\mathbf{r})^2}{\mathbf{1}^{\mathrm{T}}\mathbf{R}^{-1}\mathbf{1}}\right], \tag{21}$$

where $\hat{\mu}$ and $\hat{\sigma}^2$ are the estimated values of undetermined coefficients μ and σ^2:

$$\hat{\mu} = \frac{\mathbf{1}^{\mathrm{T}}\mathbf{R}^{-1}\mathbf{y}}{\mathbf{1}^{\mathrm{T}}\mathbf{R}^{-1}\mathbf{1}}, \tag{22}$$

$$\hat{\sigma}^2 = \frac{(\mathbf{y} - \mathbf{1}\hat{\mu})^{\mathrm{T}}\mathbf{R}^{-1}(\mathbf{y} - \mathbf{1}\hat{\mu})}{n}, \tag{23}$$

where

$$r_i = \mathrm{Corr}[\epsilon(\mathbf{x}), \epsilon(\mathbf{x}^i)]. \tag{24}$$

3.1.2 *Acquisition function*

Acquisition function is the key component of the SML, which determines the selection of each update point. For any unknown point $\mathbf{x}$, KRG provides the predicted value $\hat{y}(\mathbf{x})$ as well as the standard deviation of the predicted value $s(\mathbf{x})$. On the one hand, it can be chosen the minimum value of KRG prediction $\hat{y}(\mathbf{x})$ as the update point. On the other hand, it can

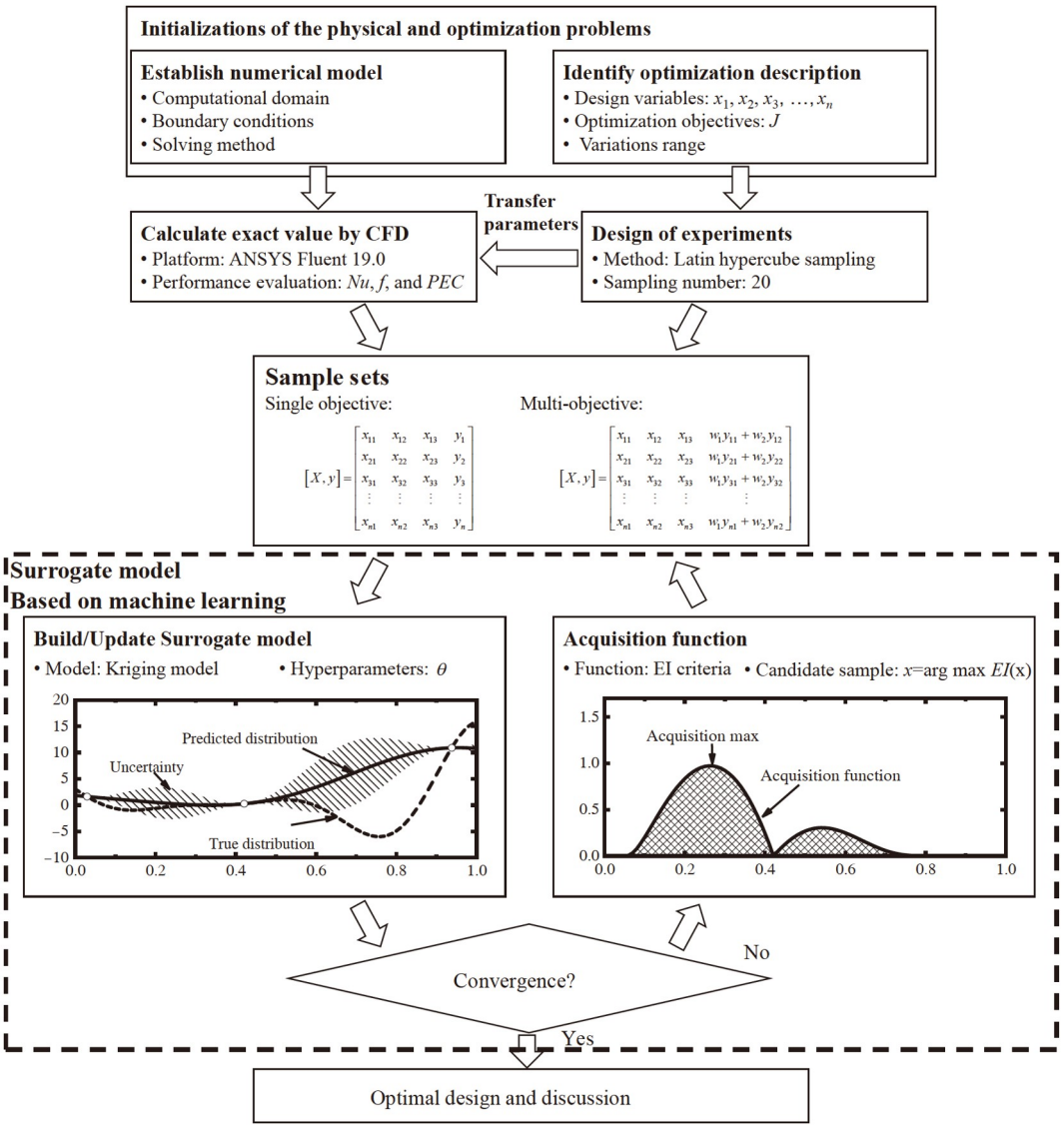

Figure 4 Framework for establishing dynamic surrogate model.

be selected the maximum value of the standard deviation $s(\mathbf{x})$ of KRG as the update point. Selecting the minimum value as the update point can fully explore the region near the current optimal solution and further improve the current optimal solution, but such a search may make the update points fall into some local optimal point. Selecting the maximum value of $s(\mathbf{x})$ as the update point can explore the unknown region as much as possible, and the update point is selected in the region where the sampling points are sparse so that the search skips out of the local region, but such a search is very time-consuming and requires a large number of additional update points to find the optimal solution of the original problem.

The Expected improvement (*EI*) criteria provide a good balance of these two search models. For an unknown point $\mathbf{x}$, it can be considered as a random variable conforming to a normal distribution with the mean $\hat{y}(\mathbf{x})$ and standard deviation $s(\mathbf{x})$:

$$Y(\mathbf{x}) \sim N(\hat{y}(\mathbf{x}), s(\mathbf{x})). \tag{25}$$

If the minimum value of the current prediction is $f_{\min}$, the improvement of the exact value of an unknown point $\mathbf{x}$ to the current optimal solution can also be seen as a random variable:

$$I(\mathbf{x}) = \max[f_{\min} - Y(\mathbf{x}), 0]. \tag{26}$$

The physical meaning of the *EI* function is the expectation of this improved value.

$$EI(\mathbf{x}) = \int_{-\infty}^{f_{\min}} (f_{\min} - Y) \frac{1}{\sqrt{2\pi}\, s(\mathbf{x})} \exp\left(-\frac{\hat{y}(\mathbf{x})^2}{2s(\mathbf{x})^2}\right) \mathrm{d}Y. \tag{27}$$

Solving this equation yields an expression for the *EI* function as

$$EI(\mathbf{x}) = \left(f_{\min} - \hat{y}(\mathbf{x})\right)\Phi\left(\frac{f_{\min} - \hat{y}(\mathbf{x})}{s(\mathbf{x})}\right) + s(\mathbf{x})\phi\left(\frac{f_{\min} - \hat{y}(\mathbf{x})}{s(\mathbf{x})}\right), \quad (28)$$

where $\Phi(\cdot)$ and $\phi(\cdot)$ denote the probability density function and cumulative distribution function of the standard normal distribution. The first term of the *EI* function increases as $\hat{y}(\mathbf{x})$ decreases, so it tends to select points with smaller prediction values as update points. The second term of the *EI* function increases as $s(\mathbf{x})$ increases, so it tends to select points with a larger prediction variance as update points. The *EI* function is a combination of these two terms, so the function will consider both points with smaller prediction values and larger variance values when selecting update points.

3.2 Optimization algorithm

Genetic algorithm is used to find the optimal value. The method converts each design variable into a binary code and treats it as a chromosome containing information. And then crossover and mutation operations are performed continuously on chromosomes inspired by the Darwinian evolution to select individuals with high fitness. The parameters of the genetic algorithm are shown in Table 1. The population size is the capacity of the initial generated individuals and is also the number of superior individuals selected from the set of parents and offspring after each evolution. The larger the population size, the greater the diversity of the population, and the more complete the optimization. However, too large a population size can result in a waste of computational resources. In this paper, we moderately choose 100 as the population size. Crossover fraction is the probability that two chromosomes in the same generation cross over, and a larger crossover fraction ensures that the genetic algorithm has a global search capability. Mutation fraction is the probability of mutation for the chromosomes in the same generation, and a small mutation rate ensures that the genetic algorithm has the ability to find the local optimum. Therefore, the crossover fraction and the mutation fraction are set to 0.8 and 0.2, respectively. Maximum generations, maximum stall generation, and termination tolerance are the termination conditions for the genetic algorithm.

Table 1 Parameters of genetic algorithm

Parameters	Value
Population size	100
Crossover fraction	0.8
Mutation fraction	0.2
Maximum generations	200
Maximum stall generation	20
Termination tolerance	10^{-6}

The values taken in Table 1 imply that the optimization is considered to converge when the change in the fitness of the optimal individual is less than 10^{-6} after 20 generations of evolution, and otherwise evolution automatically stops after 200 generations.

4 Results and discussion

4.1 Sensitivity analysis of parameters

Sensitivity analysis is firstly performed on the coordinates of control points to reduce the number of design variables and simplifying the optimization process. The curve with three control points is employed in this section for convenient analysis, and six parameters consisting of the horizontal and vertical coordinates of the three control points are extracted, namely, x_1, x_2, x_3, y_1, y_2, y_3. The parameters and the variation ranges for sensitivity analysis are shown in Figure 5. *PEC* is chosen as an evaluation indicator and is calculated by the CFD solver with Re = 10000. A six-parameter 3-level experiment designed by Taguchi method is employed, and the results are shown in Table 2, where I_i is the sum of the numerical solutions corresponding to every parameter at the ith level, i = 1, 2, 3. The range K reflects the impact degree of the parameters and is calculated as follows:

$$K = \max\{I_1, I_2, I_3\} - \min\{I_1, I_2, I_3\}. \quad (29)$$

The parameter having a higher K suggests a stronger impact on the *PEC*. As can be seen from Table 3, the impact of vertical coordinates is far greater than that of horizontal coordinates. Besides, as the number of control points increases, the variation range of the horizontal coordinates of the control points decreases, resulting in a much lower sensitivity. Therefore, only the vertical coordinates of the control points are considered as design variables in the present

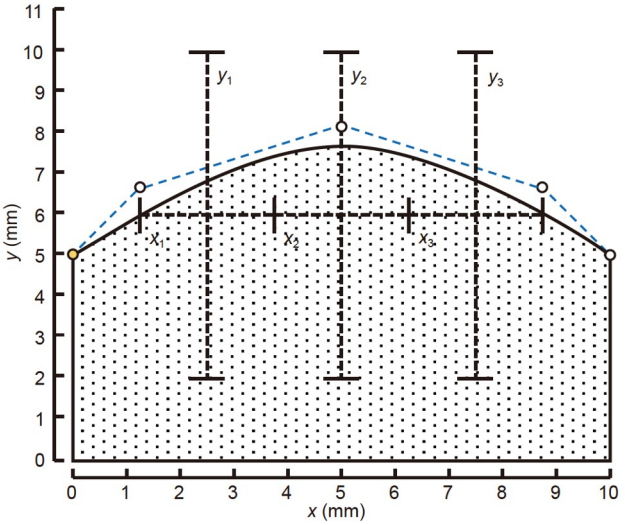

Figure 5 (Color online) Six investigated parameters and variation ranges for sensitivity analysis.

Table 2 Orthogonal test design and results

No.	x_1	x_2	x_3	y_1	y_2	y_3	*PEC*	No.	x_1	x_2	x_3	y_1	y_2	y_3	*PEC*
1	1.25	3.75	6.75	2	2	2	0.736	15	2.5	5	8.75	2	10	2	0.959
2	1.25	3.75	6.75	2	6	6	0.782	16	2.5	6.75	6.75	6	2	6	0.915
3	1.25	3.75	6.75	2	10	10	0.622	17	2.5	6.75	6.75	6	6	10	0.718
4	1.25	5	7.5	6	2	2	0.727	18	2.5	6.75	6.75	6	10	2	0.794
5	1.25	5	7.5	6	6	6	0.949	19	3.75	3.75	8.75	6	2	10	0.877
6	1.25	5	7.5	6	10	10	0.634	20	3.75	3.75	8.75	6	6	2	0.808
7	1.25	6.75	8.75	10	2	2	0.600	21	3.75	3.75	8.75	6	10	6	0.789
8	1.25	6.75	8.75	10	6	6	0.767	22	3.75	5	6.75	10	2	10	0.681
9	1.25	6.75	8.75	10	10	10	0.560	23	3.75	5	6.75	10	6	2	0.664
10	2.5	3.75	7.5	10	2	6	0.907	24	3.75	5	6.75	10	10	6	0.666
11	2.5	3.75	7.5	10	6	10	0.651	25	3.75	6.75	7.5	2	2	10	0.607
12	2.5	3.75	7.5	10	10	2	0.623	26	3.75	6.75	7.5	2	6	2	1.003
13	2.5	5	8.75	2	2	6	0.726	27	3.75	6.75	7.5	2	10	6	0.721
14	2.5	5	8.75	2	6	10	0.645	–	–	–	–	–	–	–	–

Table 3 Sensitivity analysis results

Index	x_1	x_2	x_3	y_1	y_2	y_3
I_1	6.378	6.796	6.578	6.802	6.776	6.915
I_2	6.937	6.652	6.821	7.212	6.988	7.222
I_3	6.817	6.684	6.733	6.118	6.367	5.994
K	0.560	0.144	0.244	1.094	0.621	1.228

study, considering the control points uniformly distributed in the horizontal direction.

4.2 Optimization process analysis and validation

As shown in Figure 6, three graphs show the optimization process using SML with three vertical coordinates as optimization parameters and PEC_{opt} as the optimization objective. Figure 6(a) shows the variation of the PEC_{opt} based on SML with the number of updates, N_a. With the increase of N_a, PEC_{opt} varies accordingly, which keeps unchanged until the number of updates reaches $N_a = 23$. The optimization process continues to perform until the termination condition is satisfied at $N_a = 42$ that the PEC_{opt} has not changed in the 20 updates before termination and EI_{max} is less than 10^{-4}. Figure 6(b) gives the change of EI_{max}. As the optimization proceeds, EI_{max} decreases gradually indicating that the improvement potential of the model decreases. Figure 6(c) shows the changes in design variables corresponding to PEC_{opt}. It can be seen that the optimal distribution of design variables is determined once the PEC_{opt} is stabilized, and the final optimal parameters is y_1 = 6.487 mm, y_2 = 3.707 mm, y_3 = 5.891 mm.

A validation process needs to be executed firstly to determine the superiority of SML in optimization accuracy. The exact optimal solution is obtained by the method of genetic algorithm coupled with the CFD solver (GACS), which utilizes the CFD solver to calculate the fitness value of the population generated by the genetic algorithm. The comparison is given in Table 4, and the optimization result obtained by SML is consistent with those obtained by GACS, which proves that the obtained result is accurate and does not fall into the local optimum. In the optimization process based on SML, a total of 62 points are sampled, of which 20 points are derived from the initial LHS sampling, and 42 points are added to update the model to make the optimization process finally converge. To compare with the traditional Kringing model (TKM), 62 points are directly sampled using the LHS method to build a TKM. Prediction and optimization are performed based on TKM and the comparison is also shown in Table 4. The result obtained by SML has fewer errors and is closer to the true optimal value than that obtained by TKM with the same number of sample points. This is because most sample points of SML are more targeted and more gathered near the optimal value, which ensures the prediction accuracy near the optimal value. On the other hand, the sample points of TKM are uniformly distributed, so some local features cannot be accurately expressed, leading to a reduction in local prediction accuracy.

Additionally, to address the different requirements applied in the engineering, a multi-objective optimization is performed to obtain the best compromise solutions under different weights between the heat transfer capacity *Nu* and the flow resistance factor *f*. The optimal value can be obtained by weighted summation of the normalized values for two objectives. By modifying the weight factor, a Pareto frontier can be obtained by SML. To verify its accuracy in multi-objective optimization, it is compared with the Pareto frontier set obtained by NSGA-II [68] coupled with the CFD solver method. The comparison in Figure 7 proves the re-

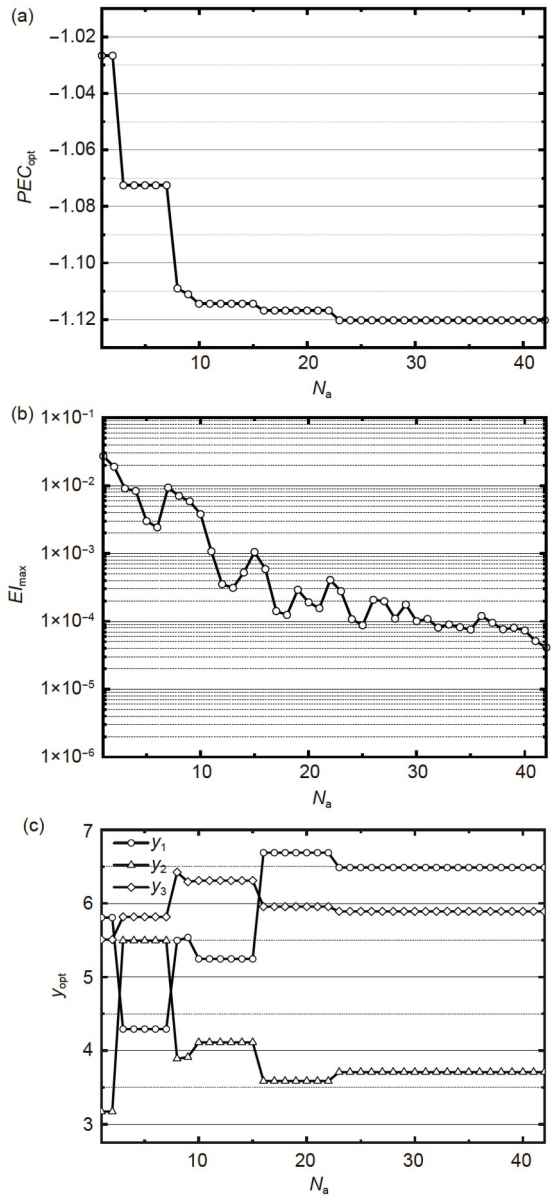

Figure 6 The process of searching the optimal *PEC* with the dynamic surrogate model. (a) PEC_{opt} with updating number N_a; (b) EI_{max} with updating number N_a; (c) optimal variables with updating number N_a.

liability of the optimization process based on the weights and the SML method.

4.3 Single objective optimization analysis

As the optimization method is validated, in this section, a single objective optimization is performed with the *PEC* as the objective to investigate the proper number of control points, the best profile for corrugated tubes, and its flow and heat transfer characteristics.

4.3.1 Effect of control points number

From eqs. (1)–(4), the generation of B-spline is significantly related to the control point number, n. The larger n is, the more profiles the B-spline can characterize. Therefore, in this section, the curves with $n = 3$, $n = 5$, $n = 7$ are employed to investigate the effects of n on the best profile and the optimal comprehensive performance, PEC_{opt}, at $Re = 10000$.

Table 4 Comparisons of the accuracy and efficiency with different methods

Method	y_1	y_2	y_3	*PEC*
SML	6.48707	3.70765	5.89107	1.12028
GACS	6.48932	3.70819	5.89205	1.12043
TKM	7.51836	2.88367	6.58953	1.07092

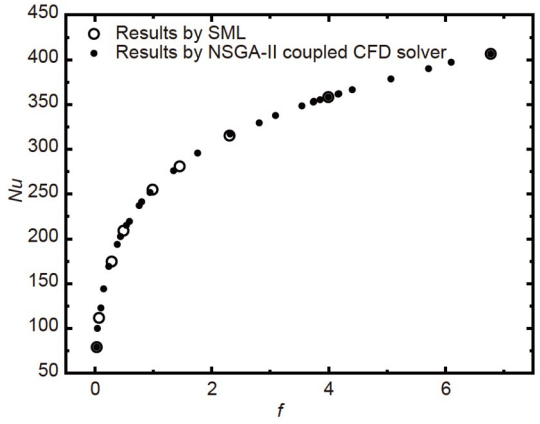

Figure 7 Validation for the multi-objective optimization.

The optimal curves and the vertical coordinates with different n obtained by SML are given in Figure 8. It gives that as n increases, the transition of the best profile is smoother and the control points are closer to the curve. The comparison shows that the difference between the optimal profiles with $n = 5$ and $n = 7$ is not significant, which proves that $n = 5$ is sufficient to characterize this optimal profile.

The variation of thermal-hydraulic performance for the optimal profiles is given in Figure 9. As n increases, the Nu_{opt} and f_{opt} are both reduced, but the PEC_{opt} increases, which means the curve is further optimized leading to a higher benefit of reduced flow resistance than weakness in heat transfer. The PEC_{opt} does not change after $n = 5$, which indicates that the optimization potential is almost non-existent, and $PEC_{opt} = 1.1849$ at this point.

4.3.2 Flow and heat transfer characteristics analysis

Two periodic units in the middle of the test section are selected for heat transfer and flow characteristics analysis, where the local pressure difference, ΔP_{local}, is calculated considering the starting cross-sectional pressure as the reference. Figure 10 shows the comparison of the local Nu, Nu_{local}, and ΔP_{local} along the mainstream direction over the best profiles of $n = 3$, $n = 5$, and smooth tube. And the velocity vector of the fluid in the optimal profiles at $Re =$

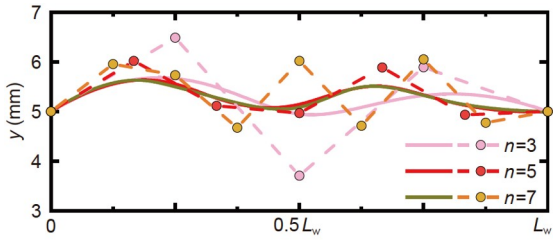

Figure 8 Variation of the optimal profiles with control points number n.

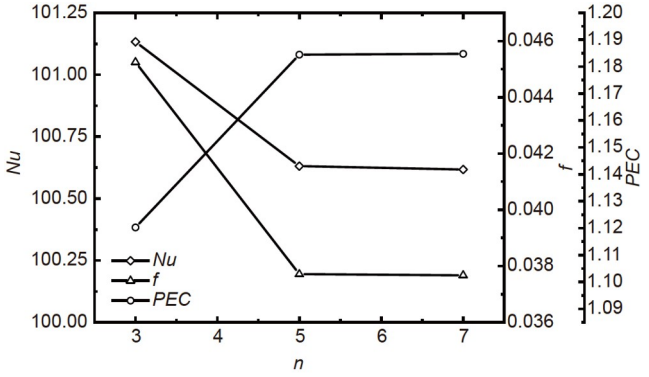

Figure 9 Variation of the performance with control points number n.

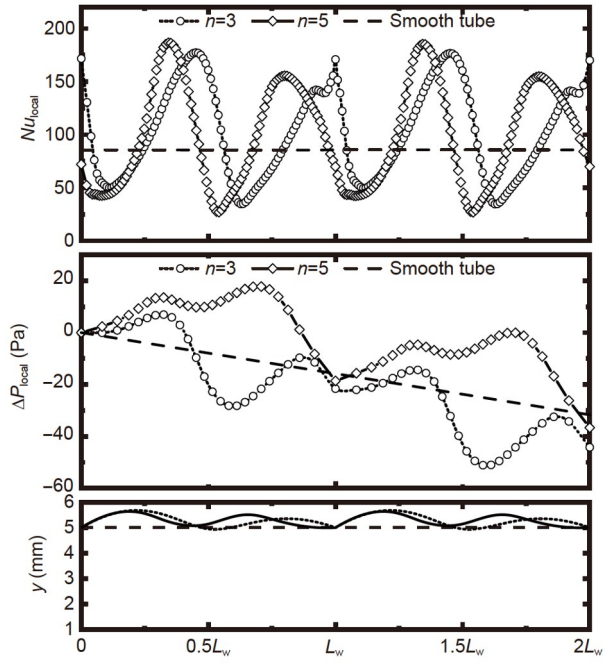

Figure 10 Nu_{local} distributions and pressure distributions for the optimal profiles.

10000 with $n = 3$ and $n = 5$ is shown in Figure 11. Owing to the sudden expanding of the tube wall, an adverse pressure gradient region is produced to reduce the fluid velocity [69,70], and the flow starts to separate from the wall inducing a reduction in heat transfer capacity even lower than that of the smooth tube. As the flow proceeds, the converging of

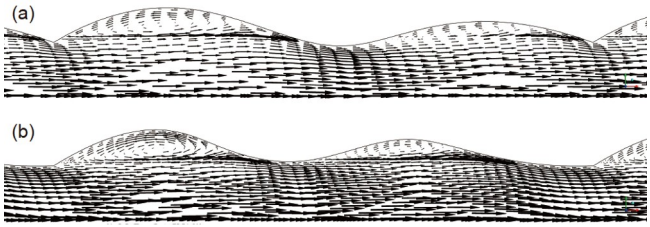

Figure 11 Velocity vector under the optimal profiles. (a) $n = 3$; (b) $n = 5$.

the tube makes the flow reattached to the wall. Because there is an angle between the mainstream direction and the converging wall, the fluid scours the wall which makes the Nu_{local} near the reattachment point increase sharply. The best profiles with $n = 3$ and $n = 5$ both are presented as a double-crest shape. Therefore, in a periodic unit, there are also two local maximum values in the distributions of Nu_{local}, and ΔP_{local}.

From the profile, the height of the first crest for the optimal curve with $n = 5$ is almost the same with $n = 3$, but the span is smaller and the downslope is steeper. Therefore, the fluid scours the wall more intensely and the first maximum Nu_{local} for $n = 5$ is higher than $n = 3$. The height of the trough for $n = 3$ is lower than the smooth tube and $n = 5$, which causes the velocity in $n = 3$ is higher and obtains a better local thermal performance in the second crest. Overall, the heat transfer performance of the enhanced tube with the optimal profile of $n = 3$ is slightly higher compared to that of $n = 5$. However, for the pump power loss, the pressure drop caused by the tube contraction is higher than the pressure increase caused by tube expansion, which makes the pump power loss larger than the smooth tube. The deeper the tube converges, the greater the pumping power loss the flow presents. Therefore, the pump power loss of the tube with the optimal profile of $n = 3$ is greater than that of $n = 5$, the pressure drop in the whole test section as shown in Figure 12.

4.3.3 Variation of the optimal profile with Reynolds number

Choosing *PEC* as the optimization objective, it is also explored for the variation of the optimal profile with the increasing *Re*. As shown in Figure 13, three optimal profiles, C_1, C_2, C_3 are obtained at $Re = 8000$, 10000, 12000, respectively. The optimal profiles keep similar that two wave crests and one wave trough exist in a design unit. The obvious difference appears in the first wave crest. As *Re* increases, the wave-amplitude of the first wave gradually gets smaller, and the profile of the corrugated tube becomes smoother. As $Re > 10000$, the variation is no longer considerable.

The performance evaluation with three profiles is shown in Figure 14. The thermal performance of three configurations all increases with the increasing *Re*. And the heat transfer

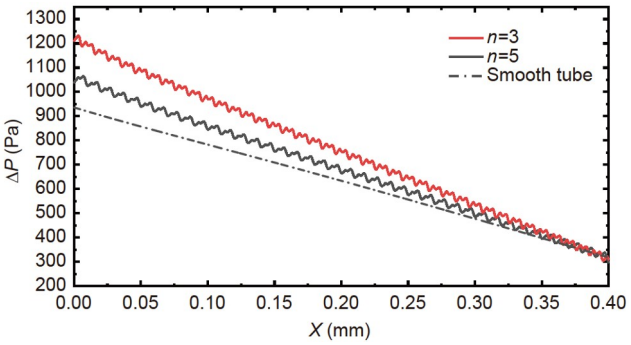

Figure 12 Pressure distributions for the optimal designs.

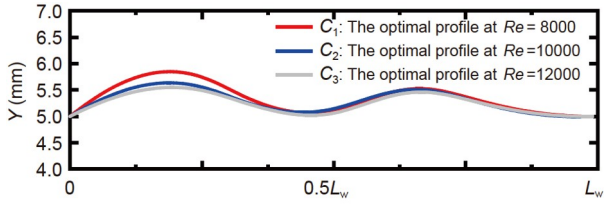

Figure 13 Variations of the optimal profiles at different Reynolds numbers.

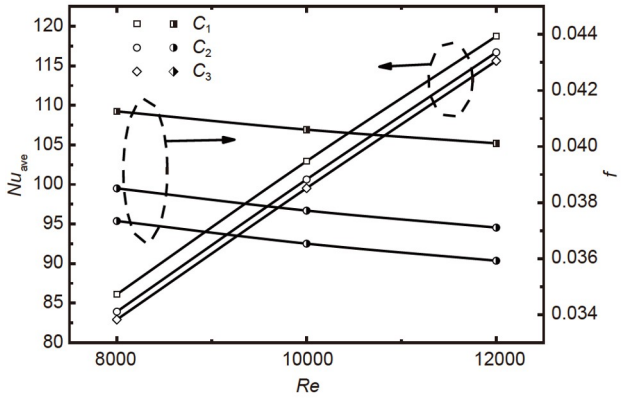

Figure 14 Thermal-hydraulic performances of the optimal profiles at different Reynolds numbers.

rate with the profile C_1 is larger than other profiles, which indicates that the improvement of heat transfer at a lower *Re* contributes to enhancing the comprehensive performance of the corrugated tube. The flow resistance of three configurations all reduces with the increasing *Re*. The smallest flow resistance appears in the profile C_3 which exhibits that as the flow velocity increases, the focus of optimization needs to gradually switch from heat transfer improvement to flow resistance reduction. Figure 15 shows the variation of *PEC* for three profiles. The PEC_{opt} decreases as the *Re* increases, where the PEC_{opt} is 1.2415 at *Re* = 8000, 1.1845 at *Re* = 10000, and 1.1504 at *Re* = 12000, respectively. The overall thermal performance studied in this paper is compared with previous studies. The cases involved in twisted oval tube reported by Tang et al. [15], transversely corrugated tube by

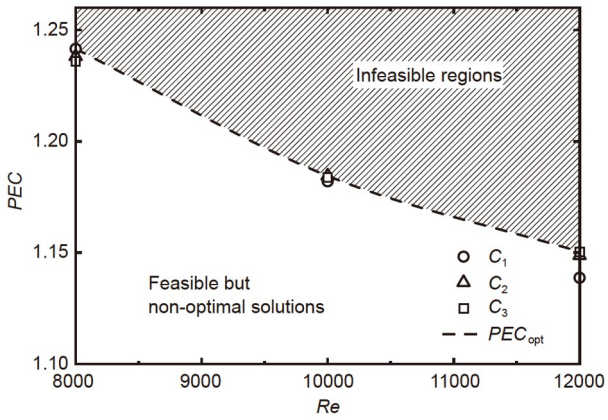

Figure 15 The optimal *PEC* distribution at different Reynolds numbers.

Mohammed et al. [17], arc-ring ribbed tube reported by Al-Obaidi and Alhamid [22], convex concave corrugated tube reported by Sadighi Dizaji et al. [71], sprially semicircle-grooved tube by Promthaisong et al. [72]. It is seen from Figure 16 that the present study possesses more considerable performance than others and exhibits a broad application prospect.

4.4 Multi-objective optimization results analysis

The optimal profile with the *PEC* as an objective gives the design with the best comprehensive performance, but the design may not meet the heat transfer or flow requirements in several situations. Improperly increasing the thermal performance of the corrugated tubes will most likely result in an additional increase in flow resistance. Therefore, in order to meet the different heat transfer and flow resistance requirements, it is necessary to make a comprehensive trade-off between two objectives, and obtain the optimization results with different weights.

4.4.1 Effect of control points number

Keeping working conditions unchanged, multi-objective optimization with $n = 3$ and $n = 5$ is carried out firstly, and the optimization results under different weights are shown in Figure 17. Every point is the optimal solution with no other points superior to it. There does not exist a point in the design space where Nu_{ave} and f get the best at the same time. Design B is a profile with the minimum flow resistance at $n = 3$ and $n = 5$, corresponding to a smooth tube. Design A is the optimum profile considering only the heat transfer performance under $n = 3$. The maximum $Nu_{ave} = 406.600$ with the maximum $f = 6.772$. Design A′ is the best point considering only the heat transfer performance under $n = 5$ with $Nu_{ave} = 418.912$, which is 3.028% better than $n = 3$, indicating that the potential of heat transfer enhancement for the corrguated tube is improved with the increasing n. This is particularly

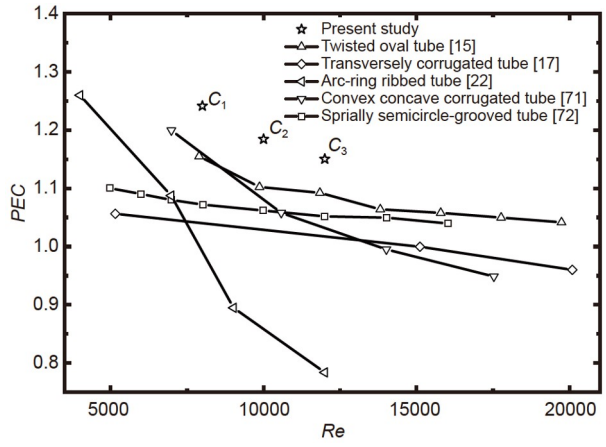

Figure 16 Comparisons of *PEC* in present study with previous research.

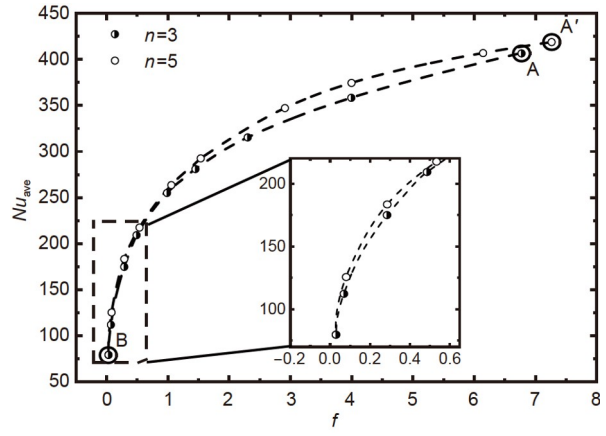

Figure 17 The optimal dominant solutions with different *n*.

useful in some cases with high requirements for heat transfer. At the same time, the corrugated tube with $n = 5$ obtained a higher thermal performance when the flow resistance is the same as A, and this exhibits the excellent performance of the corrugated tube with $n = 5$. The corresponding profiles as well as the Nu_{local} distribution are shown in Figure 18. It can be seen in the figure that the upstream half of two profiles almost overlap, and the difference is mainly in the downstream half. And combined with the Nu_{local} distribution, it can be inferred that the change with $n = 5$ in downstream half weakens the local heat exchange but strengthens the local heat exchange in the upstream half of the next design unit.

4.4.2 *Designs with different weight considerations*

The designs with two objective weights $(w_1, w_2) = (0.2, 0.8)$, (0.4, 0.6), (0.6, 0.4), (0.8, 0.2), are selected for heat transfer and flow characteristics analysis. As shown in Figure 19, as the heat transfer weight w_1 gets larger and the flow resistance weight w_2 gets smaller, the optimal y_1, y_2, y_3, y_4, y_5 then become progressively smaller. When $(w_1, w_2) = (0.2, 0.8)$ and (0.4, 0.6), the optimal profile with a double-trough structure

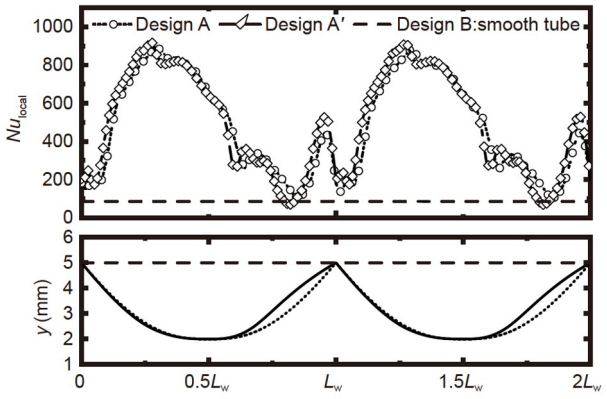

Figure 18 Nu_{local} distributions and the profiles for design A, design A′ and design B.

is present in the design unit. The presence of two troughs enhances the flow velocity of the fluid in the tube, and two secondary flows are formed respectively at the connection of different design units and between two troughs. It further enhances the convective heat transfer coefficient at the expense of increasing flow resistance. Compared with $(w_1, w_2) = (0.2, 0.8)$, the trough depth is deeper and therefore the flow is more intense under the weights of $(w_1, w_2) = (0.4, 0.6)$. When $(w_1, w_2) = (0.6, 0.4)$, and $(w_1, w_2) = (0.8, 0.2)$, the optimal profile changes from a double-trough form to a single-trough form. As w_1 increases and w_2 decreases, the trough becomes deeper. The flow develops a strong secondary flow at the corrugation unit connection, while the flow velocity also gradually increases to the maximum. Compared with the temperature distribution in Figure 20, the temperature distribution of the fluid is more uniform with the increase of w_1. This is because the deeper trough has a stronger ability to mix high temperature fluid from the wall into the core low temperature domain, which makes the heat flux diffused more fully in the fluid.

4.4.3 *Variation of the optimal set with Reynolds number*

The optimal sets of corrugated tubes under different working conditions are given in Figure 21. Visibly, the trends of Pareto solution are similar in three working conditions. In the range of $f < 1$, a great heat transfer improvement can be achieved by sacrificing a little flow resistance, and the difference between the three working conditions is not obvious enough. As f increases in the range of $f > 4$, the heat transfer improvement obtained by sacrificing the flow resistance is no longer considerable, and there is also a bigger difference in Nu for different working conditions at the same f. With the increase of Re, the minimum and maximum f are reduced, while the minimum and maximum Nu are increased, and the maximum Nu_{ave} of 358.540, 418.912, and 478.821 are acquired at $Re = 8000$, 10000, and 12000, respectively.

Technique for Order Preference by Similarity to Ideal Solution (TOPSIS) is introduced to determine the best

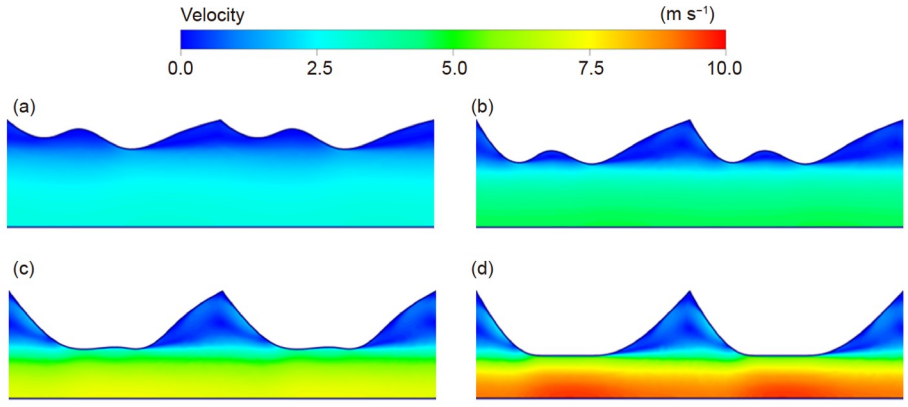

Figure 19 Velocity contours under different weighting considerations at Re = 10000. (a) w_1 = 0.2, w_2 = 0.8; (b) w_1 = 0.3, w_2 = 0.7; (c) w_1 = 0.6, w_2 = 0.4; (d) w_1 = 0.8, w_2 = 0.2.

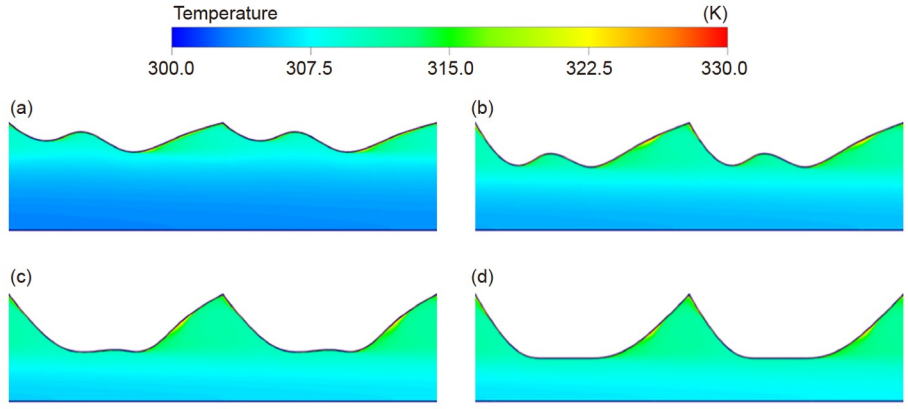

Figure 20 Temperature contours under different weighting considerations at Re = 10000. (a) w_1 = 0.2, w_2 = 0.8; (b) w_1 = 0.3, w_2 = 0.7; (c) w_1 = 0.6, w_2 = 0.4; (d) w_1 = 0.8, w_2 = 0.2.

compromise solution from the Pareto front, whose brief description is given at the end of this paper as Appendix A. And the distance from the Pareto solution to the positive-ideal solution (d_i^+) and the negative-ideal solution (d_i^-) is shown in Figure 22. By TOPSIS, the designs with (w_1, w_2) = (0.4, 0.6) are the best compromise solutions. Compared with the design with the maximum thermal performance, namely (w_1, w_2) = (1, 0), the thermal performance of the best compromise solutions is sacrificed by 36.754%, 37.088%, and 35.005% at Re = 8000, 10000, 12000, respectively. And the flow resistance of the compromise solutions is improved by 83.917%, 85.465%, and 84.473%, respectively.

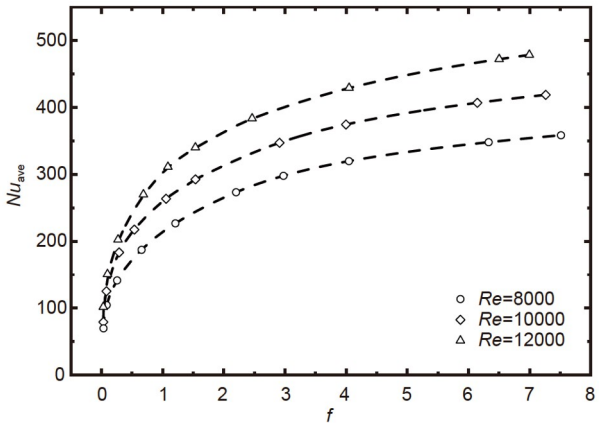

Figure 21 Optimal performances with different weights consideration under different Reynolds numbers.

5 Conclusions

The present paper mainly investigates the optimal profile of the corrugated tube by surrogate combined with machine learning technique. The surrogate model used in this paper has been verified to have considerable advantages in terms of prediction accuracy and optimization efficiency. The profiles corresponding to the optimal performance with the control point number, variable Re and different objective weights are further obtained. The conclusions can be drawn as follows.

(1) The method of surrogate based on machine learning technique is validated to have a higher prediction accuracy,

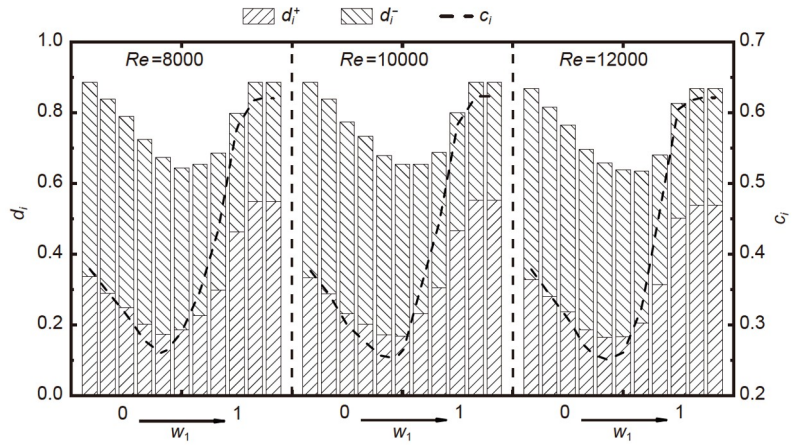

Figure 22 Distance from the Pareto solution to the positive-ideal and the negative-ideal solution.

and by this method, the desirable optimization results are obtained.

(2) The comprehensive performance of the corrugated tube is more sensitive to the vertical coordinates of the control points. As the control point number n increases from 3 to 5, the optimal *PEC* and maximum average *Nu* are both improved.

(3) The similar optimal profiles of the corrugations are obtained at different Reynolds numbers. The optimal *PEC* is 1.2415, 1.1845, and 1.1504, respectively at Re = 8000, 10000, and 12000. And the optimal shape is a double-trough shape.

(4) A multi-objective optimization is performed to meet different heat transfer or flow requirements. The best compromise solution is determined, compared to the design with the maximum thermal performance, whose thermal performance is sacrificed by 36.754%, 37.088%, and 35.005% but flow resistance is improved by 83.917%, 85.465%, and 84.473% at Re = 8000, 10000, 12000, respectively.

Appendix A: The process of TOPSIS

The process of TOPSIS to determine the best comprise solution has been briefed as follows.

Step 1 Input a decision matrix S_{mn}, and normalize S_{ij} to be the normalized value z_{ij} using the equation below, and receive a normalized matrix z_{mn}:

$$z_{ij} = \frac{S_{ij}}{\sqrt{\sum_{i=1}^{m} S_{ij}^2}}, j = 1, 2, \ldots n. \tag{A1}$$

Step 2 Determine the positive ideal solution S^+ and the negative ideal solution S^-:

$$S_j^+ = \min(z_{1j}, \ldots, z_{mj}), j = 1, 2, \ldots, n, \tag{A2}$$

$$S_j^- = \max(z_{1j}, \ldots, z_{mj}), j = 1, 2, \ldots, n. \tag{A3}$$

Step 3 Calculate the distances from the normalized value z_{ij} to the positive ideal solution S_j^+, and the negative ideal solution S_j^-, using n-dimensional Euclidean distance.

$$d_i^+ = \sqrt{\sum_{j=1}^{n} \left(z_{ij} - S_j^+\right)^2}, i = 1, 2, \ldots, m, \tag{A4}$$

$$d_i^- = \sqrt{\sum_{j=1}^{n} \left(z_{ij} - S_j^-\right)^2}, i = 1, 2, \ldots, m. \tag{A5}$$

Step 4 Calculate the relative closeness c_i to the ideal solution for each Pareto solution, which is specified as

$$c_i = \frac{d_i^+}{(d_i^+ + d_i^-)}, i = 1, 2, \ldots, m. \tag{A6}$$

Step 5 Rank the preference order and choose the best compromise solution whose relative closeness c_i is the closest to 0.

This work was supported by the National Natural Science Foundation of China (Grant Nos. 51736004, and 52076088) and the Foundation of State Key Laboratory of Coal Combustion (Grant No. FSKLCCA2007).

1 Yan C S, Xu J L, Zhu B G, et al. Numerical study on convective heat transfer of supercritical CO_2 in vertically upward and downward tubes. Sci China Tech Sci, 2021, 64: 995–1006
2 Wen Z X, Lv Y G, Li Q. Comparative study on flow and heat transfer characteristics of sinusoidal and zigzag channel printed circuit heat exchangers. Sci China Tech Sci, 2020, 63: 655–667
3 Chen L G. Progress in optimization of mass transfer processes based on mass entransy dissipation extremum principle. Sci China Tech Sci, 2014, 57: 2305–2327
4 Wang L, Xie Z H, Chen L G, et al. Equivalent thermal resistance minimization for a circular disc heat sink with reverting microchannels based on constructal theory and entransy theory. Sci China Tech Sci, 2021, 64: 111–121
5 Firoozi A O, Majidi S, Ameri M. A numerical assessment on heat transfer and flow characteristics of nanofluid in tubes enhanced with a variety of dimple configurations. Thermal Sci Eng Prog, 2020, 19: 100578
6 Zhang L, Xiong W, Zheng J, et al. Numerical analysis of heat transfer enhancement and flow characteristics inside cross-combined ellipsoidal dimple tubes. Case Studies Thermal Eng, 2021, 25: 100937
7 Lei X S, Shuang J J, Yang P, et al. Parametric study and optimization of dimpled tubes based on Response Surface Methodology and desirability approach. Int J Heat Mass Transfer, 2019, 142: 118453
8 Liao W, Liu X, Li G, et al. Evaluation of thermal-hydraulic perfor-

mance of dimpled tube from the perspective of skewness and kurtosis. Int J Thermal Sci, 2020, 156: 106469
9 Al-Obaidi A R, Chaer I. Study of the flow characteristics, pressure drop and augmentation of heat performance in a horizontal pipe with and without twisted tape inserts. Case Studies Thermal Eng, 2021, 25: 100964
10 Yadav A S, Shrivastava V, Dwivedi M K, et al. 3-dimensional CFD simulation and correlation development for circular tube equipped with twisted tape. Mater Today-Proc, 2021, 47: 2662–2668
11 Ge Y, Liu Z, Liu W. Multi-objective genetic optimization of the heat transfer for tube inserted with porous media. Int J Heat Mass Transfer, 2016, 101: 981–987
12 Shi C, Wang M, Yang J, et al. Performance analysis and multi-objective optimization for tubes partially filled with gradient porous media. Appl Thermal Eng, 2021, 188: 116530
13 Xin F, Liu Z, Zheng N, et al. Numerical study on flow characteristics and heat transfer enhancement of oscillatory flow in a spirally corrugated tube. Int J Heat Mass Transfer, 2018, 127: 402–413
14 Yu Z, Tao L, Huang L, et al. Numerical investigation on cooling heat transfer and flow characteristics of supercritical CO_2 in spirally fluted tube at various inclination angles. Int J Thermal Sci, 2021, 166: 106916
15 Tang X, Dai X, Zhu D. Experimental and numerical investigation of convective heat transfer and fluid flow in twisted spiral tube. Int J Heat Mass Transfer, 2015, 90: 523–541
16 Akyildiz F T, Siginer D A, Khezzar L. Energy losses and heat transfer enhancement in transversally corrugated pipes. Int J Heat Mass Transfer, 2011, 54: 3801–3806
17 Mohammed H A, Abbas A K, Sheriff J M. Influence of geometrical parameters and forced convective heat transfer in transversely corrugated circular tubes. Int Commun Heat Mass Transfer, 2013, 44: 116–126
18 Ajeel R K, W. Salim W S I, Hasnan K. Thermal and hydraulic characteristics of turbulent nanofluids flow in trapezoidal-corrugated channel: Symmetry and zigzag shaped. Case Studies Thermal Eng, 2018, 12: 620–635
19 Ajeel R K, Saiful-Islam W, Sopian K, et al. Analysis of thermal-hydraulic performance and flow structures of nanofluids across various corrugated channels: An experimental and numerical study. Thermal Sci Eng Prog, 2020, 19: 100604
20 Ajeel R K, Salim W S I W, Hasnan K. Numerical investigations of heat transfer enhancement in a house shaped-corrugated channel: Combination of nanofluid and geometrical parameters. Thermal Sci Eng Prog, 2020, 17: 100376
21 Ahmed M A, Yusoff M Z, Shuaib N H. Effects of geometrical parameters on the flow and heat transfer characteristics in trapezoidal-corrugated channel using nanofluid. Int Commun Heat Mass Transfer, 2013, 42: 69–74
22 Al-Obaidi A R, Alhamid J. Investigation of flow pattern, thermo-hydraulic performance and heat transfer improvement in 3D corrugated circular pipe under varying structure configuration parameters with development different correlations. Int Commun Heat Mass Transfer, 2021, 126: 105394
23 Khoshvaght-Aliabadi M, Sahamiyan M, Hesampour M, et al. Experimental study on cooling performance of sinusoidal-wavy mini-channel heat sink. Appl Thermal Eng, 2016, 92: 50–61
24 Khoshvaght-Aliabadi M. Influence of different design parameters and Al_2O_3-water nanofluid flow on heat transfer and flow characteristics of sinusoidal-corrugated channels. Energy Convers Manage, 2014, 88: 96–105
25 Zhang L, Tian L, Zhang A, et al. Effects of the shape of tube and flow field on fluid flow and heat transfer. Int Commun Heat Mass Transfer, 2020, 117: 104782
26 Pethkool S, Eiamsa-ard S, Kwankaomeng S, et al. Turbulent heat transfer enhancement in a heat exchanger using helically corrugated tube. Int Commun Heat Mass Transfer, 2011, 38: 340–347
27 Verma T N, Nashine P, Singh D V, et al. ANN: Prediction of an experimental heat transfer analysis of concentric tube heat exchanger with corrugated inner tubes. Appl Thermal Eng, 2017, 120: 219–227
28 Hong Y, Du J, Wang S, et al. Heat transfer and flow behaviors of a wavy corrugated tube. Appl Thermal Eng, 2017, 126: 151–166
29 Begag A, Saim R, Abboudi S, et al. Effect of internal and external corrugated surfaces on the characteristics of heat transfer and pressure drop in a concentric tube heat exchanger. Int J Thermal Sci, 2021, 165: 106930
30 Liao W, Luo Y, Chen T. Thermal-hydraulic performance analysis of outward convex corrugated tubes based on skewness and kurtosis. Int J Thermal Sci, 2021, 165: 106970
31 Wang S, Xiao B, Ge Y, et al. Optimization design of slotted fins based on exergy destruction minimization coupled with optimization algorithm. Int J Thermal Sci, 2020, 147: 106133
32 Zeng X, Ge Y, Shen J, et al. The optimization of channels for a proton exchange membrane fuel cell applying genetic algorithm. Int J Heat Mass Transfer, 2017, 105: 81–89
33 Ge Y, Wang S, Liu Z, et al. Optimal shape design of a minichannel heat sink applying multi-objective optimization algorithm and three-dimensional numerical method. Appl Thermal Eng, 2019, 148: 120–128
34 Ge Y, Shan F, Liu Z, et al. Optimal structural design of a heat sink with laminar single-phase flow using computational fluid dynamics-based multi-objective genetic algorithm. J Heat Transfer, 2018, 140: 022803
35 Liu Z, Zeng X, Ge Y, et al. Multi-objective optimization of operating conditions and channel structure for a proton exchange membrane fuel cell. Int J Heat Mass Transfer, 2017, 111: 289–298
36 Chen C W, Lee J J, Kou H S. Optimum thermal design of microchannel heat sinks by the simulated annealing method. Int Commun Heat Mass Transfer, 2008, 35: 980–984
37 Chen K, Xing J, Wang S, et al. Heat source layout optimization in two-dimensional heat conduction using simulated annealing method. Int J Heat Mass Transfer, 2017, 108: 210–219
38 Kang M, Hwang L K, Kwon B. Computationally efficient optimization of wavy surface roughness in cooling channels using simulated annealing. Int J Heat Mass Transfer, 2020, 150: 119300
39 Liu M, Shi Y, Yan J, et al. Lattice Boltzmann simulation of flow and heat transfer in random porous media constructed by simulated annealing algorithm. Appl Thermal Eng, 2017, 115: 1348–1356
40 Peng F, Cui G. Efficient simultaneous synthesis for heat exchanger network with simulated annealing algorithm. Appl Thermal Eng, 2015, 78: 136–149
41 Dastmalchi M, Sheikhzadeh G A, Arefmanesh A. Optimization of micro-finned tubes in double pipe heat exchangers using particle swarm algorithm. Appl Thermal Eng, 2017, 119: 1–9
42 Lee W S, Kung C K. Optimization of heat pump system in indoor swimming pool using particle swarm algorithm. Appl Thermal Eng, 2008, 28: 1647–1653
43 Maleki A, Hafeznia H, Rosen M A, et al. Optimization of a grid-connected hybrid solar-wind-hydrogen CHP system for residential applications by efficient metaheuristic approaches. Appl Thermal Eng, 2017, 123: 1263–1277
44 Rao R V, Patel V K. Thermodynamic optimization of cross flow plate-fin heat exchanger using a particle swarm optimization algorithm. Int J Thermal Sci, 2010, 49: 1712–1721
45 Sadeghzadeh H, Ehyaei M A, Rosen M A. Techno-economic optimization of a shell and tube heat exchanger by genetic and particle swarm algorithms. Energy Convers Manage, 2015, 93: 84–91
46 Han H, Yu R, Li B, et al. Multi-objective optimization of corrugated tube inserted with multi-channel twisted tape using RSM and NSGA-II. Appl Thermal Eng, 2019, 159: 113731
47 Han H, Yu R, Li B, et al. Multi-objective optimization of corrugated tube with loose-fit twisted tape using RSM and NSGA-II. Int J Heat Mass Transfer, 2019, 131: 781–794
48 Wang W, Zhang Y, Li Y, et al. Numerical study on fully-developed turbulent flow and heat transfer in inward corrugated tubes with

double-objective optimization. Int J Heat Mass Transfer, 2018, 120: 782–792
49 Wang W, Zhang Y, Li Y, et al. Multi-objective optimization of turbulent heat transfer flow in novel outward helically corrugated tubes. Appl Thermal Eng, 2018, 138: 795–806
50 Wang W, Zhang Y, Lee K S, et al. Optimal design of a double pipe heat exchanger based on the outward helically corrugated tube. Int J Heat Mass Transfer, 2019, 135: 706–716
51 Yu C, Chen J, Zeng M, et al. Numerical study on turbulent heat transfer performance of a new parallel-flow shell and tube heat exchanger with sinusoidal wavy tapes using RSM analysis. Appl Thermal Eng, 2019, 150: 875–887
52 Milani Shirvan K, Mamourian M, Abolfazli Esfahani J. Experimental investigation on thermal performance and economic analysis of cosine wave tube structure in a shell and tube heat exchanger. Energy Convers Manage, 2018, 175: 86–98
53 Grabski J K, Kołodziej J A. Laminar fluid flow and heat transfer in an internally corrugated tube by means of the method of fundamental solutions and radial basis functions. Comput Math Appl, 2018, 75: 1413–1433
54 Yarmohammadi S, Mohammadzadeh K, Farhadi M, et al. Multi-objective optimization of thermal and flow characteristics of R-404A evaporation through corrugated tubes. J Energy Storage, 2020, 27: 101137
55 Moya-Rico J D, Molina A E, Belmonte J F, et al. Characterization of a triple concentric-tube heat exchanger with corrugated tubes using Artificial Neural Networks (ANN). Appl Thermal Eng, 2019, 147: 1036–1046
56 Zhou Y, Zhu J, Zhan H, et al. A bio-inspired B-Spline Offset Feature for structural topology optimization. Comput Methods Appl Mech Eng, 2021, 386: 114081
57 Bergman T L, Lavine A S, Incropera F P, et al. Fundamentals of Heat and Mass Transfer. 7th ed. New York: John Wiley & Sons, 2011. 378–399
58 Saffarian M R, Moravej M, Doranehgard M H. Heat transfer enhancement in a flat plate solar collector with different flow path shapes using nanofluid. Renew Energy, 2020, 146: 2316–2329
59 Stynes M. Finite volume methods for convection-diffusion problems. J Comput Appl Math, 1995, 63: 83–90
60 Wang W, Shuai Y, Ding L, et al. Investigation of complex flow and heat transfer mechanism in multi-tube heat exchanger with different arrangement corrugated tube. Int J Thermal Sci, 2021, 167: 107010
61 Wang W, Zhang Y, Li B, et al. Numerical investigation of tube-side fully developed turbulent flow and heat transfer in outward corrugated tubes. Int J Heat Mass Transfer, 2018, 116: 115–126
62 Lv J Y, Liu Z C, Liu W. Active design for the tube insert of center-connected deflectors based on the principle of exergy destruction minimization. Int J Heat Mass Transfer, 2020, 150: 119260
63 Gnielinski V. New equations for heat and mass transfer in turbulent pipe and channel flow. Int Chem Eng, 1976, 16: 359–368
64 Hu Q, Qu X, Peng W, et al. Experimental and numerical investigation of turbulent heat transfer enhancement of an intermediate heat exchanger using corrugated tubes. Int J Heat Mass Transfer, 2022, 185: 122385
65 Lu P, Pan J, Hong T, et al. Prediction method of bridge static deformation based on dynamic test. Struct Concrete, 2020, 21: 2533–2548
66 Cui D, Wang G, Lu Y, et al. Reliability design and optimization of the planetary gear by a GA based on the DEM and Kriging model. Reliab Eng Syst Saf, 2020, 203: 107074
67 Dammak K, El Hami A. Thermal reliability-based design optimization using Kriging model of PCM based pin fin heat sink. Int J Heat Mass Transfer, 2021, 166: 120745
68 Deb K, Pratap A, Agarwal S, et al. A fast and elitist multiobjective genetic algorithm: NSGA-II. IEEE Trans Evol Computat, 2002, 6: 182–197
69 Wang W, Shuai Y, Li B, et al. Enhanced heat transfer performance for multi-tube heat exchangers with various tube arrangements. Int J Heat Mass Transfer, 2021, 168: 120905
70 Wang W, Li B, Tan Y, et al. Multi-objective optimal design of NACA airfoil fin PCHE recuperator for micro-gas turbine systems. Appl Thermal Eng, 2022, 204: 117864
71 Sadighi Dizaji H, Jafarmadar S, Mobadersani F. Experimental studies on heat transfer and pressure drop characteristics for new arrangements of corrugated tubes in a double pipe heat exchanger. Int J Thermal Sci, 2015, 96: 211–220
72 Promthaisong P, Boonloi A, Jedsadaratanachai W. Numerical investigation on turbulent forced convection and heat transfer characteristic in spirally semicircle-grooved tube. Int J Mech Mater Eng, 2016, 11: 9–24